Proof-of-concept of magnetic pulse disassembly of adhesively bonded Aluminum 2017 T4-MARS 300 specimen

Benoit Lagain, Thomas Heuzé, Guillaume Racineux, Michel Arrigoni, Sébastien Bergey, Thibaut Paccou, Camille Chauvin

International Journal of Solids and Structures 332 (2026) 113925

Contents lists available at ScienceDirect

International Journal of Solids and Structures

journal homepage: www.elsevier.com/locate/ijsolstr

Proof-of-concept of magnetic pulse disassembly of adhesively bonded Aluminum 2017 T4-MARS 300 specimen

Benoit Lagain [a,*], Thomas Heuzé [b], Guillaume Racineux [a], Michel Arrigoni [c], Sébastien Bergey [d], Thibaut Paccou [d], Camille Chauvin [d]

[a] Research Institute in Civil and Mechanical Engineering (GeM, UMR 6183 CNRS) Ecole Centrale de Nantes, 1 rue de la Noë, F-44321 Nantes, France
[b] Univ Brest, Bretagne INP, Institut de Recherche Dupuy de Lôme (IRDL), UMR CNRS 6027, F-29200, Brest, France
[c] ENSTA, Institut de recherche Dupuy de Lôme (IRDL), UMR CNRS 6027, 29806 Brest, France
[d] CEA, DAM, GRAMAT, F-46500 GRAMAT, France

ARTICLE INFO

Keywords:
Magnetic pulse disassembly
Adhesively bonded structures
Extension of Novikov's criterion
Interfacial fracture stress
Backface velocity measurement

ABSTRACT

The design of hybrid structures in order to correctly manage the disassembly of their subcomponents has emerged as a significant demand of various industries, regarding end-of-life, maintenance or recycling purposes. Especially, laminate structures are widespread and their disassembly, without damaging layers, and with a controlled amount of energy, is a challenging task. This study presents a proof-of-concept of Magnetic Pulse Disassembly (MPD) of adhesively bonded aluminum–steel assemblies. The GEPI pulse system available at CEA Gramat, was selected as a tunable source of energy to evaluate the ability of short-duration magnetic pulses, to debond millimeter-thick assemblies on the principle of dynamic adhesion tests. The specimens, composed of aluminum 2017 T4 and MARS 300 steel bonded by a thin epoxy adhesive, were subjected to GEPI pulses and the free surface was monitored with heterodyne laser velocimetry. Ten interfacial assembly conditions were selected, including partially bonded (localized adhesive spots) and fully bonded assemblies, in which adhesive failure was observed at the interface, with various fracture patterns depending on the bonding configuration. To interpret the experimental results, various estimates of the interface's fracture strength are constructed based on extensions of Novikov's basic criterion applied to multi-material assemblies in the context of time continuous loading. The proof-of-concept is here validated, on the one hand regarding the ability to correctly predict the measured backface velocity up to the onset of interfacial failure, and on the other hand via the ability to compute the interface's fracture strength of the assembly from the measurements. The proposed approach introduces a methodology of design for disassembly under magnetic pulse loading. It also opens new perspectives for reversible joining technologies and end-of-life recycling applications.

1. Introduction

As the demand for sustainable engineering grows, developing reliable and non-destructive methods for disassembling hybrid structures has become increasingly important. The disassembly of these structures should then be considered as a constraint from their early design stage for end-of-life, maintenance or recycling purposes. Especially, laminates previously assembled via permanent bonding technologies, like adhesives or surface welding techniques, are challenging to be disassembled without damaging layers, and with a controlled amount of energy. Their small thickness-to-length ratio limits the applicability of quasi-static disassembly technologies, but fosters those that are relying on contactless approaches and dynamic effects. Indeed, stress waves can be used to probe the laminate through its thickness, especially for achieving decohesion of laminate interfaces, without causing irreversible damages to the assembled layers. The key parameter of decohesion techniques relying on stress waves depends on the ratio between the thickness of layers and the duration of the applied pressure pulse on the laminate. Laser pulse technologies (Gay et al., 2014b; Luminita et al., 2018) can be used as a composite delaminator on a variety of materials. Pulsed lasers are also successfully used for the interfacial strength assessment of adhesively bonded assemblies (Tahan et al., 2020; Takagi et al., 2024). However, due to the short duration of its pulse and its sensitivity to spot size, it is well designed to disassemble coatings of thickness of the order of 100 μm (Kormpos et al., 2023), or to assemblies whose thickness lies between 0.8 and 3 mm (Gay et al., 2014a; Boustie et al., 2007).

For thicker layers, magnetic pulse disassembly offers a promising and relevant approach, thanks to its longer pulse duration than that of

* Corresponding author.
E-mail address: benoit.lagain@icube-research.com (B. Lagain).

https://doi.org/10.1016/j.ijsolstr.2026.113925
Received 6 December 2025; Received in revised form 7 February 2026; Accepted 26 February 2026
Available online 27 February 2026

laser, yet being sufficiently short (from 1 ms to 30 ms) to address layer thicknesses of the order of some millimeters up to several centimeters. It consists in discharging into an inductor and in a short time a given quantity of electrical energy previously stored in a capacitor bank, which makes stress waves propagate within the structure by the Lorentz forces generated in neighboring electrical conductors. Although this technology requires at least a first layer which is electrically conductive, its geometrical configurations can be adapted from those already developed in magnetic pulse welding and forming (Kapil and Sharma, 2015). For instance, electromagnetic pulses were successfully used in order to induce acoustic wave in a metal/composite specimen (Sun et al., 2021). It also provides an efficient alternative to conventional disassembly methods, particularly in the context of materials that are difficult to separate mechanically or chemically at end-of-life.

Recently, the feasibility of using magnetic pulses to disassemble laminate structures was shown in Lagain et al. (2023a), where optimal disassembly conditions were obtained from the analytical solution of an optimization problem involving a simplified one-dimensional modeling in linear elastodynamics consisting of plane waves. These optimal conditions involve both a localization criterion of the tensile stress at the interface, and a maximization of it. These results were then further improved by studying via numerical simulations the influence of transverse or cross-sectional effects on the wave propagation inside the laminate (Lagain et al., 2023b) and on its disassembly conditions, because propagating waves are actually not plane ones. A bound was set on transverse dimensions in order to keep the transient solution below the applied magnetic pulse close to the one-dimensional analytical one.

Completing these first studies devoted to theoretical and numerical aspects, the present one thus aims to provide a proof-of-concept of magnetic pulse disassembly by investigating its experimental applicability, validating the predictability of the modeling, and extracting data related to the failure. Disassembly tests are conducted using the GEPI system available at CEA Gramat Hereil et al. (2004), Blanc et al. (2008), presented in Section 2, and selected for its ability to deliver high-intensity current pulses with sub-microsecond rise time, a critical condition for achieving wave-based stress localization in millimeter-scale laminates (Lagain et al., 2023b). For the sake of simplicity, adhesively bonded aluminum–steel assemblies are considered, targeting configurations relevant for defense applications. Notice that a previous work already investigated the dynamic response of adhesively bonded assemblies using amongst others the GEPI system (Laporte, 2011). The setting up of experimental tests of the current study is presented in Section 2.2. More precisely, the considered specimens consist of MARS 300 steel pellets bonded to aluminum 2017 T4 electrodes via a thin epoxy-based adhesive layer. Experimental tests are designed according to theoretical optimal conditions developed in Lagain et al. (2023a,b), combine different ratios of layer thicknesses, include partially bonded (localized adhesive spots) and fully bonded assemblies, and the backface material velocity is measured at several points via Photonic Doppler Velocimetry (PDV) (i.e. Heterodyne Velocimetry) (Mercier et al., 2006). Experimental results and discussions are addressed in Section 3. Next, Section 4 presents the construction of estimates of the interface's fracture strength from the backface velocities, which is investigated by proposing two one-dimensional analytical models set on bi-layer and tri-layer assemblies, using the method of characteristics. These estimates extend Novikov's basic criterion (Novikov et al., 1966; Antoun et al., 2006) to multi-material assemblies (de Rességuier, 2018) in the context of time continuous loading. At last, the validation of the proof-of-concept of magnetic pulse disassembly is discussed in Section 5, and relies first on the ability of the modeling to be predictive with respect to the measured backface velocity up to the onset of interfacial failure, and on the other hand on the ability to estimate the interface's fracture strength of the assembly from the measurements. The latter provides a methodology that can then allow in the long term to construct a database that could significantly improve the reliability of fracture strength predictions, providing a robust foundation for further experimental investigations and practical implementations of this technology.

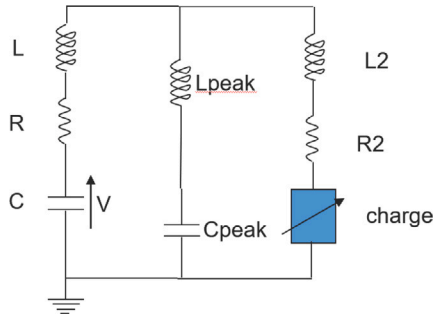

Fig. 1. Electrical representation of GEPI system.

2. Materials and methods

2.1. Low- inductance high power pulse generator

To perform magnetic pulse disassembly on laminates with a thickness suitable for ballistic protection (typically a few millimeters), the assumption of stress localization necessitates a pulse current generator operating at approximately 1 MHz for common metals such as steel or aluminum. Such a generator is available at the CEA (French Alternative Energies and Atomic Energy Commission) facility in Gramat, France.

The GEPI system is a low-inductance high-power pulse system consisting of 28 generators, which can be configured in various ways, either fully or partially connected. For a given number N of connected generators, the electrical behavior of GEPI can be modeled by the circuit depicted in Fig. 1, with the following values for capacitance, inductance, and resistance:

$$C = 0.68N \ (\mu\text{F}) \qquad L = 3.55\frac{28}{N} \ (\text{nH})$$

$$R = 3.8\frac{28}{N} \ (\text{m}\Omega) \qquad C_{peak} = 0.16N \ (\mu\text{F})$$

$$L_{peak} = 1.05\frac{28}{N} \ (\text{nH}) \qquad L_2 = 2.5 \ (\text{nH})$$

$$R_2 = 4 \ (\text{m}\Omega)$$

and V, representing the capacitor charging voltage, ranging from 70 to 85 kV, adjustable in 5 kV increments. It is important to note that the model depicted in Fig. 1 accurately applies when $N = 28$, but serves as an approximation for any case where $N < 28$. Tests reported in Section 2.3 have been conducted by connecting six generators.

In the setup known as the strip-line configuration, two flat electrodes are separated by an insulating layer composed of Mylar and Kapton films. These electrodes are locally connected at the extremity of the strips, creating a short circuit. When all the capacitors are discharged simultaneously, an electric current flows in the central region of the setup. The reachable current intensity ranges from 1 to 3.3 MA, within a rise time of about 550 nanoseconds (Hereil et al., 2004). Both the cathode and anode feature a drilled section designed to hold the sample, as illustrated in Fig. 2.

The principle of the flat transmission line relies on the flow of intense discharged currents in two parallel, plane electrodes placed face to face. Since the currents flow in opposite directions, they generate repulsive Laplace forces. Owing to the very high discharge frequency, the currents are confined within a negligible thickness compared to that of the electrode (skin effect). The resulting Lorentz forces can therefore be regarded as a surface pressure applied to the electrode surfaces. This pressure is subsequently transmitted to the samples placed on electrodes, enabling the testing of these materials against high magnetic pressures.

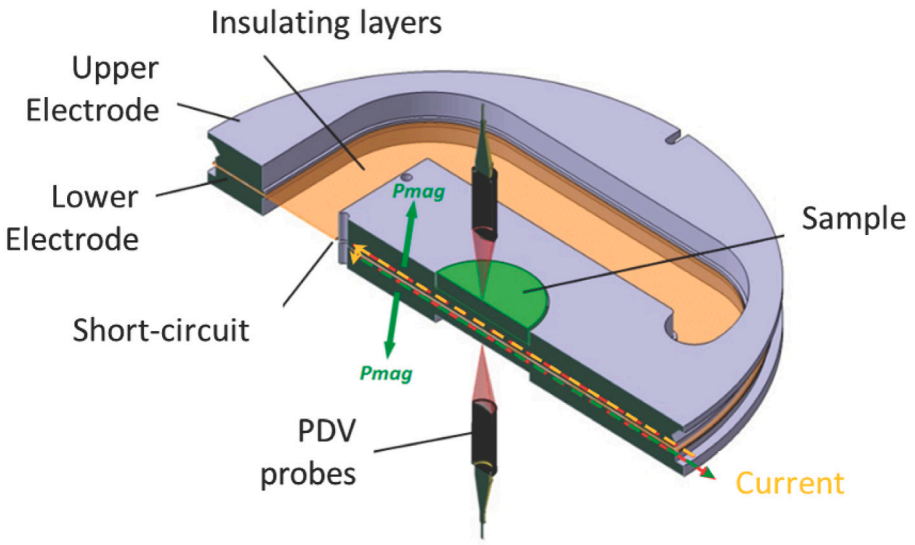

Fig. 2. GEPI's electrodes. The current flows within the skin depths of inner faces of electrodes, placed face-to-face.

2.2. Test specimens

Since the Laplace–Lorentz forces are generated within the inner skin of the GEPI electrodes, these latter can reasonably be considered as the first layer of a bi-layer laminate in the present set of experiments. Consequently, the assembly consists of two layers: the first one is the aluminum 2017 T4 electrode, designated as layer A, whose material properties are gathered in Table 1, while the second consists of a pellet made of steel MARS 300, identified as layer B, whose material properties are given in Table 2. The speed of sound of MARS 300 was experimentally measured using laser-based velocimetry. Provided a specimen of known thickness submitted to a laser pulse, the speed of sound is deduced from the measured time of wave reflections. The speed of sound of Al 2017 T4 was computed assuming an elastodynamic regime via (Wang, 2011, Eq. (7.19)), and from its material properties listed Table 1. Besides, the flatness of the usable area of the electrode is 40 µm, and surface roughness has a R_a of 0.8 µm. The surface finish was consistent among all MARS 300 samples, and rectified to the same surface roughness R_a of 0.8 µm. In order to provide an easy to set up proof-of-concept of Magnetic Pulse Disassembly, adhesive bonding was selected to build the assembly because of (i) its straightforward application, (ii) it does not necessitate modifying the layers' shapes, (iii) the adhesive bonds can be considered as interfacial joints since their thicknesses are substantially smaller than these of the two assembled layers.

The experimental specimen thus consists of a pellet of circular cross-section made of MARS 300 glued into the drilling of the electrodes. The adhesive used is the epoxy-based ARALDIT AY 103. Provided the measurements of the thicknesses of the electrode, the pellet and the stacking before and after assembly, the thickness the adhesive layer is deduced. The values for each assembly are gathered in Table 4. In a given experiment, one pellet is attached to each of the two electrodes, so that two assembly configurations can be tested at the same time during one shot. The pellet assembled with the top electrode is glued with a small spot of adhesive, while that assembled with the bottom electrode is fully bonded across its surface. Among others, Table 4 also provides the diameter of the adhesive spot of the partially bonded pellets. The diameter of the adhesive spot is determined so as to avoid any wave perturbation emanating from edges of the adhesive joint and reaching the center of the interface before decohesion has occurred, which is the main aspect considered in the present work. Using data of Tables 1, 2 and 4, the computed time associated with one wave round trip of pressure wave in the transverse direction of the adhesive joint is at least five times greater than the time of one wave round trip of pressure wave through the thickness of layer B. More precisely, the worst case is achieved for configuration 1, for which the above computed ratio is 18.12%.

Table 1
Material properties of Aluminum 2017 T4.

Quantity	Value	Unit
Mass density	2790	kg m^{-3}
Young's modulus	72.5×10^3	MPa
Poisson's ratio	0.33	[–]
Elastic speed of sound	6200	m s^{-1}
Wave impedance	17.298×10^6	N s m^{-3}
Ultimate tensile strength	427	MPa
Tensile yield strength	276	MPa
Electrical resistivity	5.15×10^{-8}	Ω m

Table 2
Material properties of MARS 300.

Quantity	Value	Unit
Mass density	7759	kg m^{-3}
Young's modulus	200×10^3	MPa
Poisson's ratio	0.3	[–]
Elastic speed of sound	5910	m s^{-1}
Wave impedance	45.8556×10^6	N s m^{-3}
Ultimate tensile strength	$\geq$ 2000	MPa
Tensile yield strength	$\geq$ 1300	MPa

Next, the procedure of gluing the sample onto the electrode starts with an accurate positioning of the sample with pieces of tape to hold it centered on the electrode. A laser pointer and optical heads are used to verify that the laser sights are indeed centered on the sample. The sample and the electrode are degreased, and a drop of adhesive is placed in the center of the electrode where the sample will be attached. The amount of adhesive is adjusted according to whether partial or complete bonding is required, and a weight of a few hundred grams is added to the sample to facilitate flow. The right dosage of adhesive was obtained after a trial and error approach, provided some preliminary tests were conducted to achieve the sought bond diameter. However, this hand-made adhesive application process can lead to variations in thickness, coverage, and consistency, potentially affecting uniformity and the bonding quality from one test to another.

Table 3
Material properties of generic Epoxy.

Quantity	Value	Unit
Mass density	1100	kg m^{-3}
Elastic speed of sound	2500	m s^{-1}
Wave impedance	2.75×10^6	N s m^{-3}

2.3. Experimental plan

The theoretical optimization conditions developed in Lagain et al. (2023a) for disassembling a bi-layer laminate consist on the one hand of a localization criterion of the tensile stress at the interface of the bi-layer laminate, expressed as

$$d_B = \frac{\tau c_B}{4}, \tag{1}$$

where d_B and c_B refer to the thickness and the speed of sound of layer B, and τ denotes the half-pseudo-period of the current generated by GEPI. On the other hand, the optimization conditions also consist of a criterion yielding its maximization, through the condition

$$\frac{d_A}{d_B} = \frac{c_A}{c_B}, \tag{2}$$

where d_A and c_A stand for the thickness and the speed of sound of pressure waves associated with layer A. Provided the rise time of the current generated by GEPI is about 550 ns (Hereil et al., 2004), combination of Eq. (1) and the elastic speed of sound c_B recalled in Table 2, the thickness of layer B should be $d_B \simeq 1.625$ mm. Besides, provided the elastic speed of sound of the electrode (see Table 1), Eq. (2) yields an optimal thickness of $d_A \simeq 1.7$ mm. However, the resulting difference between both values is approximately 0.07 mm, which is hardly compatible with the machining tolerances achievable with the available manufacturing means. As shown in Table 4, deviations of up to 0.09 mm in thickness were observed between two parts sharing the same nominal dimension. For this reason, a single nominal thickness of $d_A = d_B = 1.6$ mm was retained in practice as the optimal configuration, although it is an approximation. This approximation can be bounded as follows. Following (Lagain et al., 2023a, Eq. (26)), the difference $\Delta\sigma$ between the optimized tensile stress occurring at the interface and the actual one, achieved with the approximation of layer thicknesses, is expressed as follows

$$\Delta\sigma = K\bar{P}\left(t = \tau - 2\frac{d_A}{c_A}\right), \quad \text{with } K = \frac{2Z_B(Z_B - Z_A)}{(Z_A + Z_B)^2}, \tag{3}$$

and $\bar{P}(t)$ is the time evolution of the pressure signal applied on the assembly. The above approximation amounts to extract the value of this pressure signal at time $t = \left|\frac{\Delta d_A}{c_A}\right|$, with $\Delta d_A = (d_A)_{\text{optim}} - (d_A)_{\text{true}}$, $(d_A)_{\text{optim}}$ being the optimized value of d_A, and $(d_A)_{\text{true}}$ is the true one. From the above values, one can show that $\frac{\Delta d_A}{c_A} \simeq 0.03\frac{\tau}{2}$, where it is recalled that τ is the rising time of the loading signal till its first maximum. Accordingly, one can assess the above difference of tensile stress at the interface, relative to the maximal applied pressure $P_{\max}$, as

$$\frac{\Delta\sigma}{P_{\max}} = K\frac{\bar{P}\left(t = \left|\frac{\Delta d_A}{c_A}\right|\right)}{P_{\max}} \tag{4}$$

This relative difference is computed to be less than 1%, which is very small. Therefore, the above approximation is found valid with respect to the given objective.

Therefore, establishing a proof-of-concept of Magnetic Pulse Disassembly amounts to check experimentally the validity of the above theoretical optimal conditions. To this end, various geometrical configurations are investigated, whose geometries lie around and include the above theoretical optimal one. In particular, to control the localization of the appearance of the tensile stress through the depth of the laminate, the experimental protocol aims to vary the thicknesses of both layers A and B. The chosen thicknesses of layer A (the aluminum 2017 T4 electrode) and layer B (the MARS 300 pellets) are shown in Table 4, in such a way that unloading waves may cross either at the interface or within one of the two assembled layers, thus generating tensile stress. Table 4 also provides the peak magnetic pressure $P_{\max}$ and the diameter of the adhesive spot on the partially bonded pellet. Provided the material properties of the electrodes gathered in Table 1, and the maximal pressures applied during the tests given in Table 4, it is clear that electrodes are expected to deform in the purely elastic regime. The safety margin is all the more important if we assume a profile of plane wave, at least during the early stage of propagation, and compare the maximal pressures to the Hugoniot elastic limit computed with (Wang, 2011, Eq. 7.33).

It is important to note that modifying the thickness of layer A requires adjustments of an electrode, particularly by altering the depth of the drilling. The variation in layer thicknesses is a crucial aspect of this study, as it allows for deviations from the optimal configuration. In Table 4, configuration 5 is specifically included to test the repeatability, at least for the theoretically optimized configuration.

2.4. Current and instrumentation

GEPI capacitor bank was charged before each test at a voltage of 70 kV, which is the lowest value admissible by this generator. The charging voltage is defined to within 0.1 kV. Beyond that, there may be deviations in the final result of a few percent, which are verified by current measurement. The current intensity within the central part of the configuration is measured using a Rogowski coil. By adjusting the width of the electrodes and the intensity of the current, it is possible to control the applied magnetic pressure, achieving levels up to 80 GPa. The main idea of the present work is to take advantage of GEPI's short rise time to disassemble, yet limit the generated pressure to avoid damaging the assembled layers. Fig. 3 shows the plots of the time evolutions of the current, measured via Rogowski coils, flowing through the electrodes for all five shots. A first peak of about 1 MA is observed. A small variation of less than 5% on the first current peak can be observed. This deviation is consistent with the overall expected uncertainties of the GEPI system, and can come from the small deviation of charging voltage, small errors of measurements of the current, carried out via a Rogowski coil, and the technology of the GEPI system that is based on the use of multiple switches. Besides, provided the pseudo-period of the current shown in Fig. 3, of about 1.8×10^{-6} s, the electrical resistivity of the Aluminum electrode given in Table 1, and a relative magnetic permeability of about unity for that alloy, the skin depth within which eddy currents are flowing can be assessed with (Lagain et al., 2023a, Eq. (7)). This is evaluated to about 0.15 millimeters, which is one order of magnitude below the values of thickness of electrodes given in Table 4. Therefore, the magnetic loading can be well approximated as a surface pressure.

The experimental setup is equipped with Photonic Doppler Velocimetry (PDV) probes to measure the backface velocities of the MARS 300 steel pellets at various locations of interest. The time profile of these velocities contains an image of the interface's response. Locations of PDV probes related to top and bottom electrodes are shown in Figs. 4 and 5, respectively. On the top electrode, PDV probe 1 is aligned directly with the center of the partially bonded pellets, while PDV probe 2 is shifted from PDV probe 1 with an offset of 10 mm. PDV probe 3 is placed directly above the electrode to measure its backface velocity, which is used to deduce the loading applied on the assembly. Similarly on the bottom electrode, PDV probes 4 and 5 are placed above the bottom pellets, which are bonded over their entire surface. PDV probes 2 and 5 aim at providing additional information regarding debonding, particularly due to the cross-sectional effect.

Table 4
Experimental configurations for magnetic pulse disassembly proof-of-concept. Wave crossing at the interface can be optimized (O), or non-optimized (NO).

Shot	d_A (mm)	d_B (mm)	P_{max} (MPa)	Adhesive diameter (mm)	Thick. adh. partially bonded (mm)	Thick. adh. fully bonded (mm)	Waves crossing
1	3.99	3.08	114	14	0.005	0.011	in layer *B*
2	1.58	1.66	124	9	0.021	0.013	interface, O
3	4	1.62	115	12	0.014	0.005	interface, NO
4	4.02	0.86	122	10	0.029	0.015	layer *A*
5	1.6	1.57	124	9	0.014	0.007	interface, O

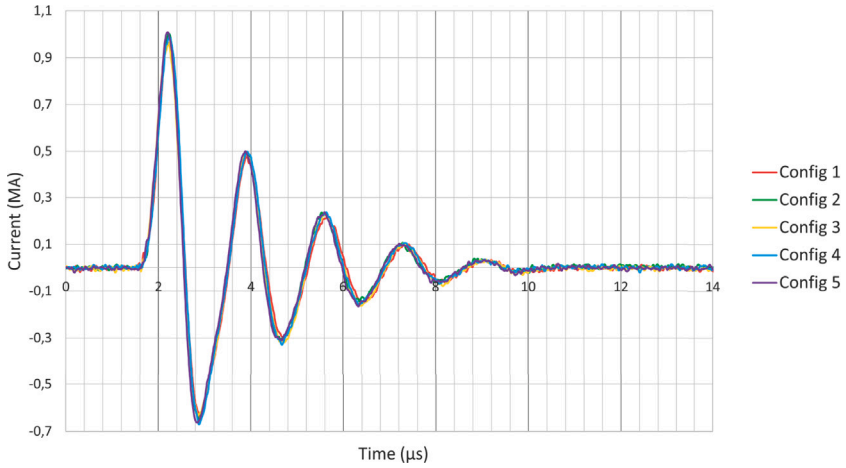

Fig. 3. Time evolution of the current flowing in the electrode during magnetic pulse disassembly experimental proof of concept for configurations described in Table 4.

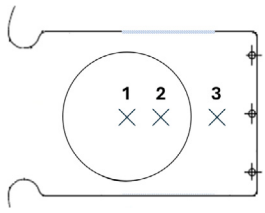

Fig. 4. Theoretical PDV-positioning on the top electrode.

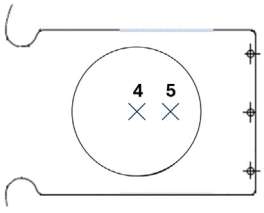

Fig. 5. Theoretical PDV-positioning on the bottom electrode.

3. Results and discussions

Five shots were conducted, allowing for the investigation of the five geometries of assembly configurations summarized in Table 4, either in fully or partially bonded states, yielding ten interfacial assembly conditions. Each of these assemblies, both partially and fully bonded specimens, was fully debonded during the experiment, indicating that none of them was able to withstand the generated interfacial tensile stress. Even used with its lowest strength capacity, GEPI facility still appears too powerful for a non-destructive testing of such adhesively bonded bi-layer laminate.

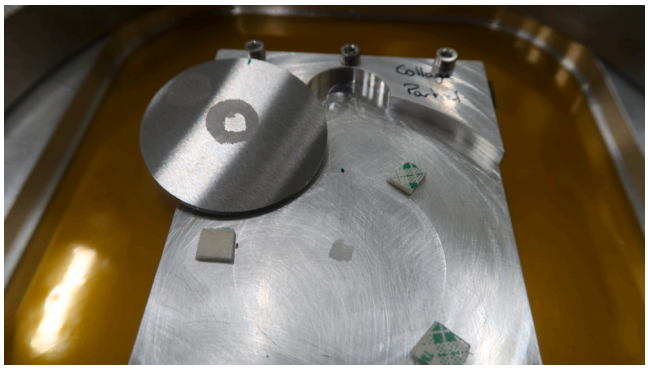

Fig. 6. Debonded steel pellet, at first in partially bonded assembly conditions.

As shown in Fig. 6, all partially bonded specimens exhibited a distinct interfacial failure pattern. For partially bonded specimens, the center of the adhesive layer remained attached to the electrode, whereas the periphery stayed stuck to the steel pellet. This phenomenon, repeated for all partially bonded specimens, was not observed in fully bonded ones. One possible explanation among many others, is that cross-sectional effects appears, via wave reflections at the adhesive joint boundaries, in an analog manner to what was already observed and studied in LASAT tests (Boustie et al., 2007).

3.1. Electrode reference signals

Fig. 7 shows the time evolutions of the backface normal velocity component of the electrode, measured by PDV probe 3, which represents the image of the applied loading since the normal pulse only propagates through the electrode (as highlighted in Fig. 4). Time zero in Fig. 7 is associated with that of triggering of the GEPI system and

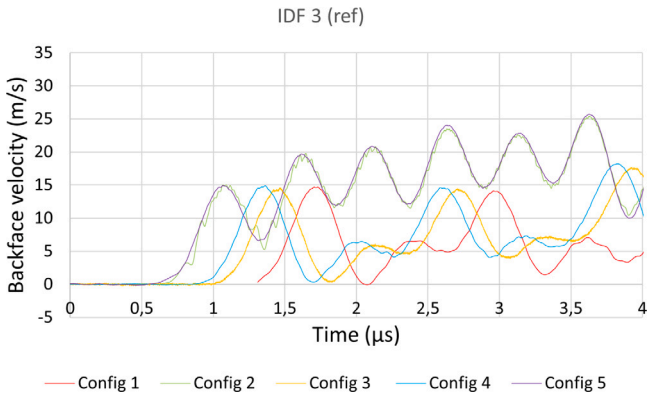

Fig. 7. Electrode's backface normal velocity measured by probe 3. Time zero is associated with the triggering of GEPI system and the measurement acquisition.

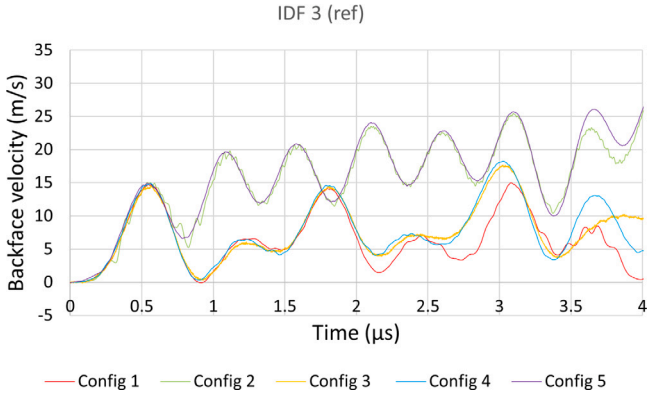

Fig. 8. Electrode's backface normal velocity measured by probe 3, realigned to match their rising front.

of the measurement acquisition, and is the same for all shots. The time delay between curves shown in Fig. 7 results from the various times of traveling of a pressure wave $\frac{d_A}{c_A} + \frac{d_B}{c_B}$ through the various thicknesses of electrodes and the various thicknesses of specimen, as summarized in Table 4. Signals of configurations 2 and 5 are close to each other, they share close geometries. Then, signals of configurations 4, 3, 1 raise successively in time as the associated specimen thicknesses increase. For readability purpose, Fig. 8 show these curves realigned based on their first rising front, so that to clearly compare their first peak. A good repeatability is observed for similar electrode geometries. In addition, the signal rise time also shows good repeatability, with a value of about $550^{+3.6\%}_{-2\%}$ ns.

Due to the very low values of backface velocities recorded (below 30 m/s), a Lissajous post-process has been used (Weng et al., 2006), using two out-of-phase signals, instead of a classical Short-Time Fourier transform (STFT) based on the PDV spectrogram. At those speeds, the signal-to-noise ratio is poor with STFT, yielding accurate results only in the vicinity of velocity peaks, but inaccurate or unreadable ones below 4 m/s. In these very low range of speed, a Lissajous treatment shows better results. Such treatment has been used for all PDV signals. Furthermore, the Lissajous provides displacement values, which can then be derived numerically to get the velocity. Especially, negative velocity can be obtained, contrary to STFT treatment based on the PDV spectrogram. Some instances of that can be observed in Fig. 9. Uncertainties also come with the post-processing via the Lissajous algorithm of PDV signals, especially when applied to low velocity signals, and also arise from the conversion from displacement to velocity, which includes a smoothing step. The proper post-process of PDV signals appears as a tradeoff between accuracy and smoothing of the signal. Too much smoothing leads to a loss of details on the signal, such as inaccurate value of signal peaks, too few smoothing provides an unreadable signal, with too much high frequency noise. Comparison with peak values of velocity obtained with STFT – in areas where it is exploitable – offers guidelines to calibrate the smoothing related to the Lissajous algorithm. Uncertainties related to post-processing the signals with the various choices of filtering and smoothing, and comparison with STFT and spectrogram extraction, can be framed within an interval of 1 m/s.

3.2. Specimens' recorded backface velocities

Figs. 9(a), 9(b), 9(c), and 9(d) show plots of the backface velocities measured by PDV probes 1, 2, 4 and 5, associated with various bonding conditions (partially/fully bonded) of the specimens, whose locations are shown in Figs. 4 and 5. Once again, to enhance clarity and readability, these curves have been realigned based on their first rising edge, with the same time delays than those identified in Fig. 7.

In Fig. 9(a), focus is made on data collected by probe 1, positioned at the center of a specimen that is partially bonded. The signal related to configuration 4 exhibits a sort of plateau after its maximum, lying in between 6 to 8 m s^{-1}. This trend is reminiscent to those of free flight already observed in LASAT tests (Tahan et al., 2020; Bolis et al., 2007), and may suggest a fast complete debonding of layer B has occurred. The time evolution after the first peak shows oscillations of small magnitude, typical of the free flight of a specimen. Besides, the time between subpeaks of oscillations is about 500 ns, and comparable to a wave round trip in layer B as described in Bolis et al. (2007). More generally, and as will be shown more precisely in Section 5.2 for configuration 2 and 5, a backface velocity signal with a lower magnitude of pullback velocity than expected in a perfect cohesion scenario can possibly be the marker of debonding (Bolis et al., 2007; Antoun et al., 2006). Other recordings show residual back-and-forth wave propagation with the same nearly constant period, and whose signals also do not go back to zero after the first unloading occurring at about 1 µs. This can be a marker of debonding between layers A and B (configurations 2, 3, and 5), for which a detailed analysis will be proposed in Section 5.2. In configuration 1, the signal returns to zero at times approximately equal to 1 and 3.5 µs, though a few oscillations in-between these two values, that can suggest a partial debonding has occurred.

Fig. 9(b) presents the velocities recorded by probe 2, located close to the edge of the partially bonded specimen. Similar trends for configurations 2 and 5 are observed as these of probe 1, though delayed in time. However, configuration 4 shows significantly lower magnitudes of backface velocity. This discrepancy can be attributed to the positioning of the adhesive spot on the pellet, which is not perfectly centered, as evidenced in Fig. 6. The off-center placement of the adhesive spot implies that probe 2, depending on its exact location, may not be directly aligned with the joint between the pellet and the electrode resulting in a bad wave transmission and at adhesive joint. Especially, the signal of configuration 4 remains a long time close to zero, which appears quite inconsistent with the signal recorded by probe 1, lying 10 mm away. Hence this recorded signal should rather be disregarded.

Fig. 9(c) illustrates the velocities recorded by probe 4, positioned at the center of the fully bonded specimen. Globally, similar trends are observed than these of probe 1, up to a few points of interest. First, the signal of configuration 1 goes back to zero periodically, at times approximately equal to 0.9, 2 and 3 µs, contrary to the signal of PDV 1. This can possibly be a marker of cohesion of the interface, related to a higher joint strength, because the adhesive has been distributed over the whole cross-sectional area of the specimen. Next, the second maximum of the signal associated with configuration 5 is higher than the first one, which is reminiscent to what was already observed in the time evolution of the interfacial normal stress component, computed with two-dimensional numerical simulations carried out on fully bonded specimen in Lagain

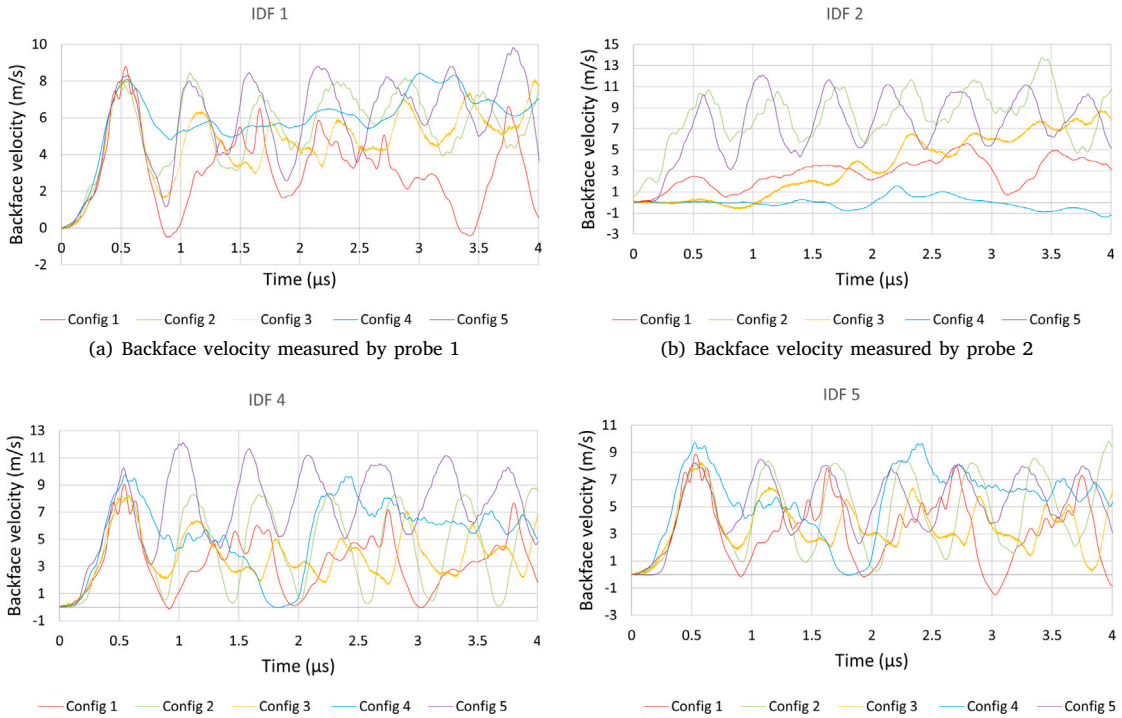

(a) Backface velocity measured by probe 1

(b) Backface velocity measured by probe 2

(c) Backface velocity measured by probe 4

(d) Backface velocity measured by probe 5

Fig. 9. Backface velocity measured during Magnetic Pulse Disassembly tests.

et al. (2023b, see Fig. 10 and 22). It translates the effects of transverse wave propagation onto the maximum peak values. Third, the signal of configuration 4 appears now more plausible than that recorded by probe 1, shown in Fig. 9(a). Combined with the suspicious one recorded by probe 2, it may confirm that something nonconforming occurred during the testing of the partially bonded configuration 4. Notice also that the signal of configuration 4 in fully bonded interface (Fig. 9(c)) goes back to zero at time approximately equal to 3.8 μs, suggesting a possible incomplete debonding.

Complementing this, Fig. 9(d) displays measurements from probe 5, located 10 mm away from the center of the fully bonded specimen. It is worthwhile to observe that probes 4 and 5 recorded similar (and unshifted) signals due to (i) similar local adhesively bonded interface conditions, (ii) a wave front close to being a plane one, and (iii) minimal cross-sectional effects at least during the early stages of the response.

The recorded backface velocities across different configurations reveal distinct behaviors for each assembly, allowing for a clear distinction in how each one responds under experimental conditions. Notice that the velocities measured by probes 1 and 4 are of particular interest, since they are consistent with assumptions which have been considered in modeling either developed in Lagain et al. (2023a) or in Lagain et al. (2023b).

4. Interface's fracture strength

4.1. Novikov's basic criterion

The criterion of Novikov (Novikov et al., 1966) (see also (Antoun et al., 2006, Chap. 4)) can be employed to estimate the spall fracture stress in a spalling experiment from the pullback velocity identified in the time evolution of the backface velocity, if an acoustic assumption holds. This criterion, relying on the method of characteristics, demonstrates that the difference between the first peak and the first local minimum observed in the backface velocity, combined with an assumption of constant material impedance Z, can be used to compute the fracture stress. Recall that the impedance $Z = \rho c$ is defined as the product of the speed of sound and the density of the given material.

The underlying principle is that a stress wave generated by an impact propagates through the material and reflects from the free surface. The interaction between the reflected and incoming unloading waves generates a tension state which induces a local fracture if sufficiently high. This fracture manifests as a distinct backface velocity profile. The difference between the first velocity peak and the subsequent local minimum represents the influence of the spall fracture on the backface velocity. By using this velocity difference, referred to as the "pullback" velocity, along with the constant acoustic impedance of the material, the fracture stress can be determined. This approach assumes that the material is homogeneous, meaning it has uniform mechanical properties (acoustic impedance), and that the stress wave propagates under uniaxial strain conditions. Additionally, it presumes that fracture occurs when the tensile stress at a given point exceeds the material's fracture strength.

Extension of Novikov's criterion to bi-layer multi-material assemblies has been addressed in de Rességuier (2018), employing a model based on discontinuous wave interactions. In contrast, the present analysis deals with a system of continuous waves generated by the time continuous magnetic pulse loading. Furthermore, the presence of interfaces between the assembled materials, such as an adhesive layer, introduces additional complexity. These interfaces may exhibit distinct mechanical properties, and while a thin interface might have a negligible influence on the elastodynamic wave propagation, it could be crucial in determining the tensile strength of the assembly. Given the continuous nature of wave propagation and the presence of an intermediate layer, the approach proposed in de Rességuier (2018) should be adapted.

4.2. Extension of Novikov's criterion to a bi-layer multi-material system with time continuous loading

In contrast to the assumed discontinuous loading considered in Novikov's criterion, a time continuous loading, especially one with a

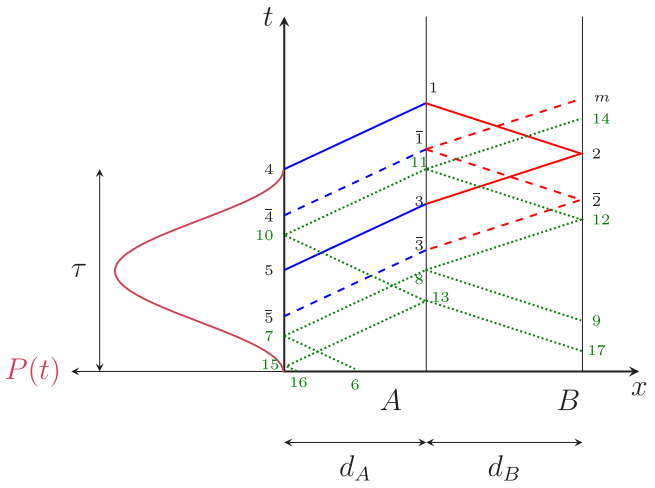

Fig. 10. Characteristic plane (x,t) associated with a bi-layer laminate, of layers (A,B), submitted to a continuous pulse loading of time duration τ on its left end. Such configuration corresponds to that named A_0B_1 in Lagain et al. (2023a). Solid lines describe characteristic lines propagating in layer A (in blue) and B (resp. in red), involved in the computation of the state of point 1, which represents the theoretically maximal achievable tension. Dashed lines refer to these associated to the fracture state $\bar{1}$, whose tension level already reached the interface's fracture strength. Densely dotted green lines are devoted to the computation of the backface velocity *before* failure occurs.

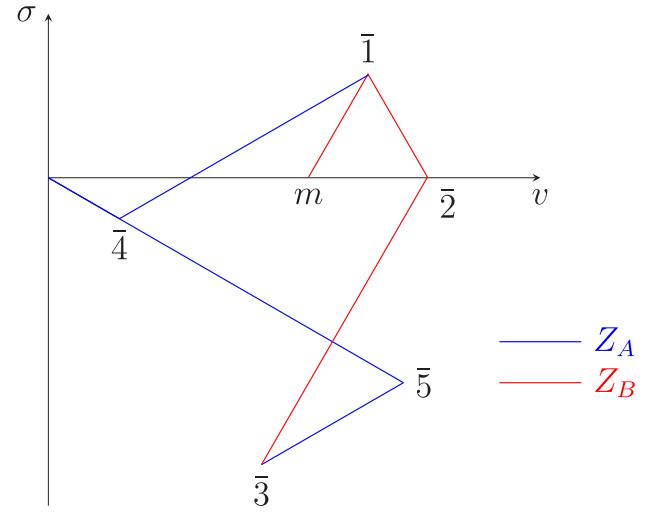

Fig. 11. Phase plane (v,σ) associated with the dashed characteristic lines lying in the characteristic plane shown in Fig. 10, plotted assuming $Z_A/Z_B < 1$.

non-constant increase rate, disrupts the correlation between the maximum backface velocity and the occurrence of fracture. More precisely, the maximum backface velocity is considered to occur in Novikov's criterion when the shock front traveling rightward reaches the backface, so that the associated unloading wave is directly related to the coordinates (x,t) of occurrence of the fracture via a negative characteristic line. However in case of a time continuous loading, especially applied on a bi-layer laminate, the negative characteristic line that connects the right free boundary to the fracture location no longer propagates the maximum backface velocity. Rather, this negative characteristic line relates the fracture occurrence to an earlier (and lower) value of this backface velocity. Consequently, the maximum backface velocity is no longer a valid reference value to compute the interfacial fracture strength.

Fig. 10 shows the characteristic plane (x,t) (or Lagrange diagram) associated with a bi-layer laminate, of layers (A,B), submitted to a continuous pulse loading of time duration τ on its left end. In order to fix ideas, and without loss of generality, a half-period of square sine is represented as loading time evolution whose maximal (state 5) and release values (state 4) lead, through characteristic (solid) lines $5-3$ and $4-1$ in layer A and $3-2$ and $2-1$ in layer B, to a theoretically maximal achievable tension level in state 1. However, it is likely that this maximal tension value will never be actually reached as it may exceed the maximal interface fracture strength. Rather, fracture between both layers may thus occur before state 1, at state $\bar{1}$, which is connected to analog states $\bar{4}$ and $\bar{5}$ via the dashed characteristic lines, which do not correspond to the maximal loading and release values. Formally, state $\bar{1}$ may occur between states 3 and 1 depending on the ratio of thicknesses d_A/d_B and of material impedances Z_A/Z_B of the two layers.

Fig. 11 shows the phase plane (v,σ), denoting the longitudinal velocity and stress components respectively, associated with the dashed characteristic lines represented in the characteristic plane shown in Fig. 10. The slopes between states are here associated with the two material impedances Z_A, Z_B with the same color coding than that used in Fig. 10, considering here $Z_A/Z_B < 1$. Indeed, states in the phase space are connected together via characteristic equations

$$d\sigma = \pm Z_k dv,\ k \in \{A,B\} \tag{5}$$

valid along characteristic lines

$$dx = \pm c_k dt,\ k \in \{A,B\} \tag{6}$$

holding for both rightward $(+)$ and leftward $(-)$ propagating waves. Integrating (5) between two states $(i,j) \in \{\bar{1},\dots,\bar{5},m\}$ gives

$$\sigma_i - \sigma_j = \pm Z_k (v_i - v_j),\quad k \in \{A,B\}. \tag{7}$$

Formally, $v_{\bar{4}}$ can be positive or negative according to the ratios of thicknesses d_A/d_B and of material impedances Z_A/Z_B of the two layers, while its stress value will still be negative. Next, for most configurations, one can show that $\sigma_{\bar{3}} < \sigma_{\bar{5}}$. Then, the difference in material impedances, the traction-free conditions at boundary states $\bar{2}$ and m, and the unloading wave propagating along the characteristic line $\bar{4}-\bar{1}$ combine to yield a tensile stress at state $\bar{1}$.

From the viewpoint of the measurement of the backface velocity, the state $\bar{1}$ is connected to backface ones m and $\bar{2}$ through positive and negative characteristic lines. In essence, the information of the fracture occurred at the interface at state $\bar{1}$ arrives at the end of the laminate at time t_m. State m also corresponds to a local minimum of the backface velocity, essentially because the subsequent velocity time profile will account for a newly created free boundary at the interface, or at least a softened interface because it would have been damaged, that will make re-increase the backface velocity. Fig. 12 shows a synchronized time sequence of events occurring at both the interface and the backface of the laminate. The time evolution of the loading applied on the left end is also superposed with these related to the interface, for a complete understanding of the time sequence of events. The time t_m associated with state m, usually extracted for application of Novikov's criterion, is thus easy to extract from the experimental signal. It is delayed by $\Delta t = \frac{d_B}{c_B}$ after the interface stress has reached its maximal strength, and breaks or starts to soften. Possibly, the interface may follow a damaging process before breaking, during which the interfacial stress decreases continuously from its maximal tensile strength value σ_R to zero. When the latter vanishes, the time rate of the velocity profile increases sharply. Two successive sharp changes of the second time derivative of the backface velocity profile is thus the image of a continuous damaging process of the interface. Next, according to the characteristic plane shown in Fig. 10, the time associated with the state $\bar{2}$ precedes that of state m of a delay of $2\frac{d_B}{c_B}$, that is one wave round trip within layer B. Fig. 12 clearly shows that state $\bar{2}$ no longer corresponds

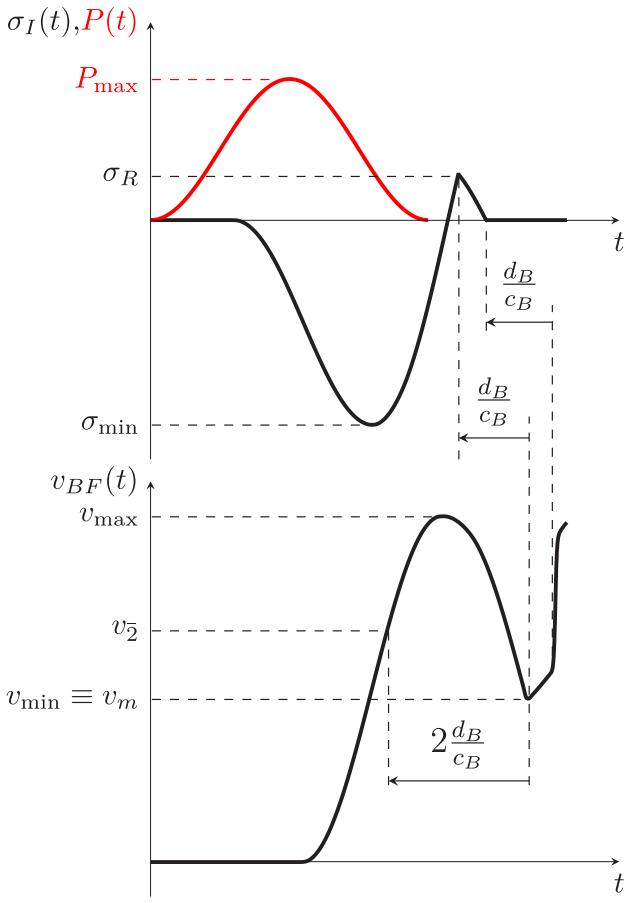

Fig. 12. Time evolutions of the pressure loading $P(t)$, the interfacial stress $\sigma_I(t)$ and the backface velocity $v_{BF}(t)$, considering fracture of the interface occurs in tension at point $\bar{1}$.

to the maximal backface velocity, but to an early-in-time velocity value, yet larger than v_m.

Applying the characteristic Eqs. (7) to characteristic lines connecting points $\bar{2}$ and $\bar{1}$, as well as to the line connecting points $\bar{1}$ and m, results in the following equations:

$$\sigma_{\bar{1}} - \sigma_{\bar{2}} = -Z_B(v_{\bar{1}} - v_{\bar{2}}) \tag{8}$$

$$\sigma_m - \sigma_{\bar{1}} = Z_B(v_m - v_{\bar{1}}) \tag{9}$$

Provided the right free boundary conditions $\sigma_m = \sigma_{\bar{2}} = 0$ are enforced, the combination of Eqs. (8) and (9) yields the expression of an estimate of the interfacial fracture strength

$$\sigma_{\bar{1}} = \frac{Z_B}{2}(v_{\bar{2}} - v_m) \approx \sigma_R. \tag{10}$$

Hence, the mathematical expression used to compute σ_R is identical to that of Novikov's criterion, but applied with an extracted velocity value $v_{\bar{2}}$ which is different, and occurring at a time $2\frac{d_B}{c_B}$ upwind that of the local minimum v_m of the backface velocity. Notice also that, depending on the ratio of thicknesses d_A/d_B and of material impedances Z_A/Z_B of the two layers, the times of occurrence of the minimal stress $\sigma_{\min}$ and the maximal backface velocity $v_{\max}$ may not be simply delayed by the propagation time of a pressure wave $\frac{d_B}{c_B}$ through the thickness of layer B.

4.3. Extension of Novikov's criterion to a tri-layer multi-material system, including a thickened interface, based on a two-scale characteristic analysis

In the (debonded) specimen shown in Fig. 6, an adhesive layer is added to bond the pellet onto the electrode, to build the laminate.

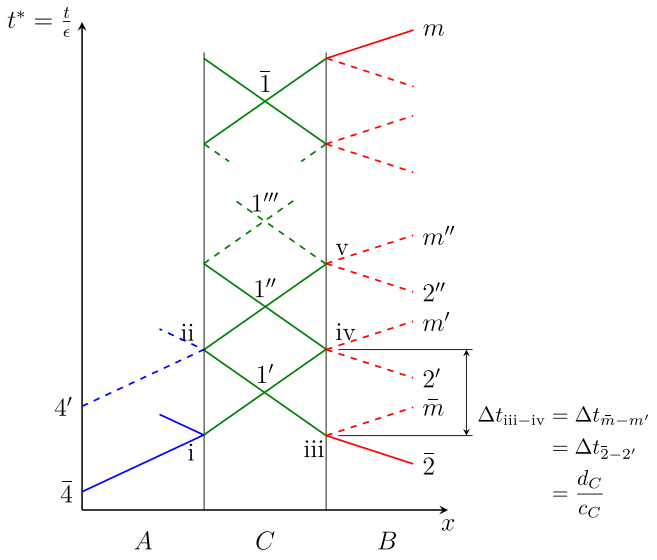

Fig. 13. Zoomed characteristic plane (x, t^*) about state $\bar{1}$, plotted with two thick layers (A, B) and a third one C much thinner than the two others.

This adhesive layer can be considered as a third one introduced between layers A and B, though significantly thinner than the other two. From a macroscopic perspective it can be shown that, if the dominant wavelength is significantly greater than the layer thickness, this thin layer can be neglected if the description of wave propagation through the laminate is of primal interest. Indeed, due to its small thickness, multiple wave reflections occur within it during a very short time, quickly leading to its mechanical equilibrium. However, its presence may be crucial when determining the fracture strength of the interface.

It is possible to derive a refined estimate of the fracture tensile strength σ_R, improved with respect to that provided by Eq. (10), by considering the presence of a third, thinner (adhesive) interfacial layer. To this end, a two-scale analysis can be performed locally in the vicinity of state $\bar{1}$ in the characteristic plane (see Fig. 10), where interfacial fracture is expected to occur. Provided a given small parameter $\epsilon > 0$, one can define a local time coordinate such that $t^* = \frac{t}{\epsilon}$. Fig. 13 shows the characteristic plane (x, t^*) zoomed in the vicinity of state $\bar{1}$, as well as the expected solution. Labels of additional interfacial states have been named $\text{i}, \text{ii}, \text{iii}, \text{iv}, \text{v}$. Input characteristic lines $\bar{4} - \text{i}$ and $\bar{2} - \text{iii}$ result, after a set of wave reflections within layer C of thickness far smaller than the two others, in a rightward characteristic line in layer B joining state m. Making the small parameter tend so that $\epsilon \to 0$, it is expected to retrieve the solution shown in Fig. 10. In order to build an improved estimate of the interfacial fracture strength, each intermediate mechanical state, either within layer C or at its interfaces with layers A and B are likely to yield fracture, earlier than state $\bar{1}$ would do.

On the one hand, cohesive failure can occur, within the adhesive layer rather than at any adhesive/substrate interface. Hence, fracture may take place at states $1'$, $1''$, $1'''$, etc., which are generated within the adhesive layer due to the crossing of unloading waves and associated reflections. Fig. 14 shows the phase plane (v, σ) associated with the characteristic one shown in Fig. 13, in a scenario where $Z_C \ll Z_A < Z_B$. Due to the strong impedance mismatch between the three layers, it is clearly observed that intermediate states $1'$, $1''$, $1'''$ converge towards $\bar{1}$ after multiple wave reflections within layer C, and they all lie on the characteristic equation joining states $\bar{1}$ to m. Hence, in the scenario of a cohesive failure, each of these intermediate states appear as improved estimates of the interfacial fracture strength with respect to $\sigma_{\bar{1}}$, given by Eq. (10).

On the other hand, adhesive failure can occur, meaning that it takes place at the interface between the adhesive and one of the two

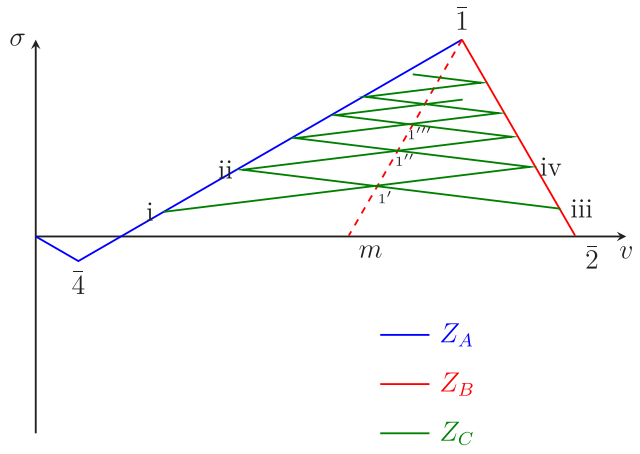

Fig. 14. Phase plane (v, σ) associated with the characteristic plane shown in Fig. 13, for a three-layer laminate, plotted in the scenario $Z_C \ll Z_A < Z_B$.

substrates. If it occurs at the interface between layers A and C, states i, ii and subsequent ones lying on the blue characteristic equation connecting states $\bar{4}$ and $\bar{1}$ in Fig. 14 are potential candidates. If the adhesive failure occurs at the interface between layers C and B, then states which are potential candidates for failure are iii, iv and subsequent ones lying on the red characteristic equation connecting states $\bar{2}$ to $\bar{1}$.

A post-mortem analysis of the broken specimen allows one to know if cohesive or adhesive failure has occurred, and with what substrate in the latter case. However, it is not obvious in each scenario to determine what intermediate state has led to fracture of the "macroscopic" interface between layers A and B. In this work, a conservative approach is followed to build this refined estimate of interfacial fracture strength, that consists of considering that fracture has occurred via first intermediate states, namely state $1'$ for a cohesive failure, or states ii and iii, iv for adhesive failures with substrates A and B respectively. Notice that for the sake of simplicity, mechanical state (i) is disregarded as its computation would rely on using recursively a set of characteristic lines lying in layer A, leading to a complicated analytical expression, while others can be easily connected to the known states of the backface, the determination of their analytical expression is therefore more straightforward. The stress values of these first intermediate states will then provide estimates which are lower bounds of the interfacial fracture strength. Hence, they will allow, together with Eq. (10), to frame that interfacial fracture strength.

4.3.1. Fracture stress related to cohesive failure

The longitudinal velocity and stress components at specific points within the characteristic plane shown in Fig. 13 can be determined using integrated characteristic Eqs. (7) between two points connected by a characteristic line. Moreover, the right free boundary condition enforces:

$$\sigma_i = 0\,, \qquad i = \{\bar{2}, 2', 2'', \bar{m}, m', m'', m\}. \tag{11}$$

Applying Eq. (7) to the characteristic lines between states iv and $1'$, as well as between states $1'$ and iii, results in:

$$\sigma_{\mathrm{iv}} - \sigma_{1'} = Z_C(v_{\mathrm{iv}} - v_{1'}) \tag{12}$$

$$\sigma_{1'} - \sigma_{\mathrm{iii}} = -Z_C(v_{1'} - v_{\mathrm{iii}}) \tag{13}$$

Combining Eqs. (12) and (13), $\sigma_{1'}$ can be expressed as follows:

$$\sigma_{1'} = \frac{1}{2}(\sigma_{\mathrm{iii}} + \sigma_{\mathrm{iv}} + Z_C(v_{\mathrm{iii}} - v_{\mathrm{iv}})). \tag{14}$$

Then, characteristics equations relating states iv $- 2'$ and iv $- m'$ results in:

$$\sigma_{m'} - \sigma_{\mathrm{iv}} = Z_B(v_{m'} - v_{\mathrm{iv}}) \tag{15}$$

$$\sigma_{\mathrm{iv}} - \sigma_{2'} = -Z_B(v_{\mathrm{iv}} - v_{2'}) \tag{16}$$

Similarly, characteristics equations relating states iii $-\bar{2}$ and iii $-\bar{m}$ yield

$$\sigma_{\mathrm{iii}} - \sigma_{\bar{2}} = -Z_B(v_{\mathrm{iii}} - v_{\bar{2}}) \tag{17}$$

$$\sigma_{\bar{m}} - \sigma_{\mathrm{iii}} = Z_B(v_{\bar{m}} - v_{\mathrm{iii}}) \tag{18}$$

Next, inserting Eqs. (15) and (17) in Eq. (14), and accounting for the right free boundary condition $\sigma_{m'} = \sigma_{\bar{2}} = 0$ (see Eq. (11)), then $\sigma_{1'}$ can be expressed as follows:

$$\sigma_{1'} = \frac{Z_B}{2}(v_{\bar{2}} - v_{m'}) + \frac{(Z_C - Z_B)}{2}(v_{\mathrm{iii}} - v_{\mathrm{iv}}). \tag{19}$$

Looking at Eq. (19), its first contribution $\frac{Z_B}{2}(v_{\bar{2}} - v_{m'})$ can be identified to Novikov's criterion (Novikov et al., 1966) applied to continuous loadings, that is Eq. (10), provided $v_{m'}$ replaces v_m in the sense that it corresponds now to the identified local minimum on the time evolution of the backface velocity because the interface will have broken earlier. Next, the second contribution $\frac{(Z_C - Z_B)}{2}(v_{\mathrm{iii}} - v_{\mathrm{iv}})$ can be considered as a corrective one due to the introduction of layer C in the laminate.

Combining now Eqs. (15) and (16), v_{iv} is given by:

$$v_{\mathrm{iv}} = \frac{v_{m'} + v_{2'}}{2}. \tag{20}$$

From the combination of Eqs. (17) and (18), v_{iii} reads:

$$v_{\mathrm{iii}} = \frac{v_{\bar{m}} + v_{\bar{2}}}{2}. \tag{21}$$

Thus, inserting Eqs. (20) and (21) in Eq. (19), $\sigma_{1'}$ can be expressed as follows:

$$\sigma_{1'} = \frac{Z_B}{2}(v_{\bar{2}} - v_{m'}) + \frac{(Z_C - Z_B)}{4}(v_{\bar{m}} + v_{\bar{2}} - v_{m'} - v_{2'}). \tag{22}$$

Some analog reasoning, especially involving characteristic equations relating states $1''$ – iv and $1''$ – v, allows us to get the expression of the stress expression of the second intermediate state $\sigma_{1''}$:

$$\sigma_{1''} = \frac{Z_B}{2}(v_{2'} - v_{m''}) + \frac{(Z_C - Z_B)}{4}(v_{m'} + v_{2'} - v_{m''} - v_{2''}), \tag{23}$$

as well as the associated velocity

$$v_{1''} = \frac{v_{\mathrm{iv}} + v_{\mathrm{v}}}{2} + \frac{\sigma_{\mathrm{iv}} - \sigma_{\mathrm{v}}}{2Z_C}. \tag{24}$$

4.3.2. Fracture stress related to adhesive failure

Combination of Eqs. (17) and (18) gives σ_{iii}, the first interfacial stress at the $C - B$ interface

$$\sigma_{\mathrm{iii}} = \frac{Z_B}{2}(v_{\bar{2}} - v_{\bar{m}}). \tag{25}$$

and the combination of Eqs. (15) and (16) give the second one as

$$\sigma_{\mathrm{iv}} = \frac{Z_B}{2}(v_{2'} - v_{m'}). \tag{26}$$

Regarding the interface between layers A and C, the determination of state i would require more informations to be computed, but the next one, state ii, can be easily deduced writing characteristics equations relating states ii – iii and ii – v:

$$\sigma_{\mathrm{ii}} - \sigma_{\mathrm{iii}} = -Z_C(v_{\mathrm{ii}} - v_{\mathrm{iii}}) \tag{27}$$

$$\sigma_{\mathrm{v}} - \sigma_{\mathrm{ii}} = Z_C(v_{\mathrm{v}} - v_{\mathrm{ii}}) \tag{28}$$

Next, combining Eqs. (27) and (28), σ_{ii} reads:

$$\sigma_{\mathrm{ii}} = \left(\frac{(Z_C + Z_B)}{4}(v_{\bar{2}} - v_{m''}) + \frac{(Z_B - Z_C)}{4}(v_{2''} - v_{\bar{m}})\right) \tag{29}$$

It is possible to deduce one estimate of the interfacial fracture tensile stresses in adhesive failure scenarii, either at the $A-C$ (given by σ_{ii}) or at the $C - B$ (given by σ_{iii} or σ_{iv}) interfaces, from the time evolution of the backface velocity by extracting from this measurement the values of $v_{\bar{m}}, v_{\bar{2}}, v_{m'}, v_{2'}, v_{2''}, v_{m''}$.

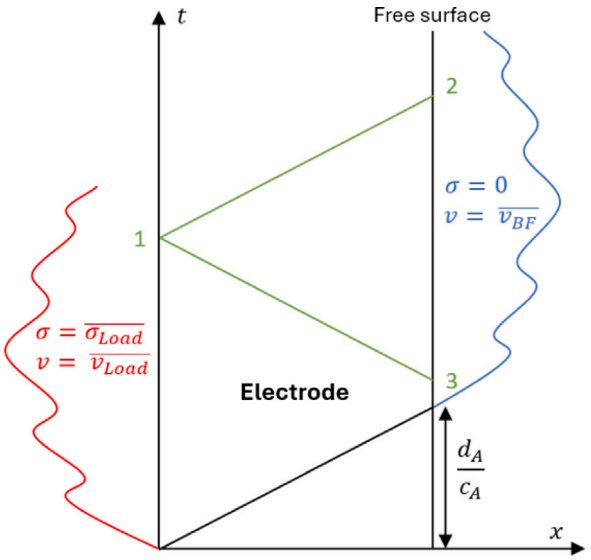

Fig. 15. Lagrange diagram in the (x,t) plane, showing some characteristic lines connecting the front and rear faces of the electrode.

5. Validation of proof-of-concept of magnetic pulse disassembly

To validate the proposed proof-of-concept, this section applies the analytical framework developed in Lagain et al. (2023a) and in Section 4 to the experimental results presented in Section 3. The proof-of-concept of magnetic pulse disassembly is here evaluated according to two main criteria. The first one is the ability of the linear elastodynamic modeling of the bilayer laminate (introduced in Lagain et al. (2023a)) to predict with sufficient accuracy the measured backface velocity up to the onset of interfacial failure. This means that experiments initially designed from that modeling actually behave as expected because of this good agreement. The second one relies on bi-layer and tri-layer models introduced in Section 4, that allow to provide estimates of the interface's fracture strength using extended Novikov criterion. Although they do not allow to predict the occurrence of failure, they provide here a methodology to build in the long term a database of fracture strength depending on the geometrical configuration and the couple of assembled materials, which then will allow to be able to predict disassembly, and then to experience the concept of magnetic pulse disassembly. The analysis presented here focuses on configurations where tensile stress is expected to localize at the interface, allowing a direct and meaningful application of the proposed methodology.

5.1. Reconstruction of the time evolution of the loading

The mechanical loading generated by GEPI magnetic discharge can be reconstructed from the backface velocity recorded by PDV probe 3. The reconstruction is here made easier because relatively low-pressure loading levels are applied on the electrodes during these experimental tests. As a consequence, the method of characteristics described in Section 4.2 is relevant for this reconstruction. Under the assumption of linearity, the material wave impedance Z remains constant, allowing the backface velocity signals to be traced along constant characteristic lines without difficulty, as illustrated in Fig. 15.

Provided the backface velocity v_{BF} is a measured quantity at the right free end of an aluminum electrode of thickness d_A and material wave impedance Z_A, it is possible to deduce the applied loading at point 1 from known states at points 2 and 3. Integrating characteristic Eq. (5) along characteristic lines joining states 1-2 and 1-3 yields

$$\sigma_2 - \sigma_1 = Z_A(v_2 - v_1) \tag{30}$$

$$\sigma_1 - \sigma_3 = -Z_A(v_1 - v_3) \tag{31}$$

Provided the right free boundary, one gets $\sigma_2 = \sigma_3 = 0$. Thus, the stress at point 1 can be directly related to the measured velocity profile:

$$\sigma_1 = Z_A \frac{v_3 - v_2}{2}. \tag{32}$$

This approach allows for the determination of the input loading by post-processing the backface velocity in conjunction with the electrode's parameters. Consequently, the reconstructed applied stress is given by:

$$\bar{\sigma}_{load}(t) = \begin{cases} \dfrac{Z_A\left[v_{BF}\left(t - \frac{d_A}{c_A}\right) - v_{BF}\left(t + \frac{d_A}{c_A}\right)\right]}{2} & \text{if } t > \dfrac{d_A}{c_A} \\ -\dfrac{Z_A v_{BF}\left(t + \frac{d_A}{c_A}\right)}{2} & \text{if } t \le \dfrac{d_A}{c_A} \end{cases} \tag{33}$$

Fig. 16 presents the time evolution of the stress loading reconstructed for each configuration over the first 3 µs, with all signals adjusted to start simultaneously for clarity.

5.2. Comparison of experimental and analytical backface velocities before failure

Applying the characteristics Eqs. (7) to characteristic lines connecting points 6 and 7 represented in Fig. 10 results in the following equations:

$$\sigma_7 - \sigma_6 = -Z_A(v_7 - v_6) \tag{34}$$

Provided the natural initial conditions, σ_6 and v_6 are equal to zero, yielding

$$v_7 = -\frac{\sigma_7}{Z_A}. \tag{35}$$

Then, applying the characteristics Eqs. (7) to characteristic lines connecting points 8 and 9, and points 8 and 7, results in the following equations:

$$\sigma_8 - \sigma_9 = -Z_B(v_8 - v_9) \tag{36}$$

$$\sigma_8 - \sigma_7 = Z_A(v_8 - v_7) \tag{37}$$

Provided the right free boundary condition, σ_9 is zero, and v_9 is also zero because of the natural initial conditions and that the state 9 occurs before the first pressure wave reaches the backface of the assembly. The combination of Eqs. (35), (36) and (37) yields:

$$v_8 = -\frac{2\sigma_7}{Z_A + Z_B} \tag{38}$$

$$\sigma_8 = \frac{2Z_B\sigma_7}{(Z_A + Z_B)} \tag{39}$$

Thus considering points 12, 8 and 10, 13 yields:

$$\sigma_{12} - \sigma_8 = Z_B(v_{12} - v_8) \tag{40}$$

$$\sigma_{10} - \sigma_{13} = -Z_A(v_{10} - v_{13}) \tag{41}$$

whose combinations with (39) gives

$$v_{12} = -\frac{4\sigma_7}{Z_A + Z_B} \tag{42}$$

$$v_{10} = -\frac{\sigma_{10}}{Z_A} - \frac{\sigma_{13}(Z_A - Z_B)}{Z_A Z_B} \tag{43}$$

However, state 13 may not vanish for every couples of geometries, materials and time evolution of the loading. It can thus be recursively connected to states 15, 16, 17. States 16,17 vanish because of natural initial conditions or they are not yet perturbed by any pressure wave. The stress in state 15 is known by the left boundary condition. From the above, the following equations can be written

$$\sigma_{13} = -Z_B v_{13} \tag{44}$$

$$\sigma_{13} - \sigma_{15} = Z_A(v_{13} - v_{15}) \tag{45}$$

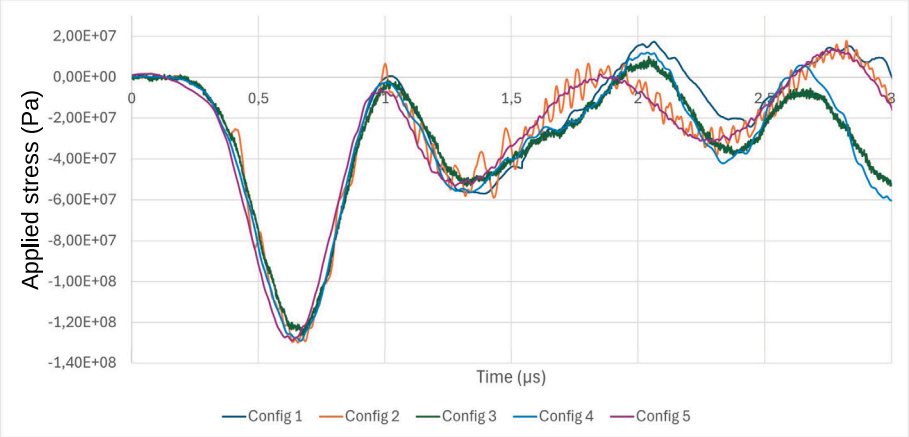

Fig. 16. Time evolution of the reconstructed stress loading for each configuration.

$$\sigma_{15} = -Z_A v_{15} \tag{46}$$

which, when combined with Eq. (43), yields

$$v_{10} = -\frac{\sigma_{10}}{Z_A} - \frac{2\sigma_{15}(Z_A - Z_B)}{Z_A(Z_A + Z_B)} \tag{47}$$

Now considering points 11 and 10 yields:

$$\sigma_{11} - \sigma_{10} = Z_A(v_{11} - v_{10}) \tag{48}$$

$$\sigma_{11} - \sigma_{12} = -Z_B(v_{11} - v_{12}) \tag{49}$$

which combination gives the velocity and stress at point 11 as follow:

$$v_{11} = -\frac{4Z_B\sigma_7}{(Z_A + Z_B)^2} - \frac{2\sigma_{10}}{Z_A + Z_B} - \frac{2\sigma_{15}(Z_A - Z_B)}{(Z_A + Z_B)^2} \tag{50}$$

$$\sigma_{11} = -\frac{4Z_B Z_A\sigma_7}{(Z_A + Z_B)^2} + \frac{2\sigma_{10}Z_B}{Z_A + Z_B} + \frac{2\sigma_{15}Z_B(Z_A - Z_B)}{(Z_A + Z_B)^2} \tag{51}$$

Finally, applying the characteristic Eqs. (7) to characteristic lines connecting points 14 and 11 results in the following equations:

$$\sigma_{14} - \sigma_{11} = Z_B(v_{14} - v_{11}) \tag{52}$$

Provided the right free boundary conditions $\sigma_{14} = 0$ yielding

$$v_{14} = \frac{4(Z_A - Z_B)\sigma_7}{(Z_A + Z_B)^2} - \frac{4\sigma_{10}}{Z_A + Z_B} + \frac{4\sigma_{15}(Z_A - Z_B)}{(Z_A + Z_B)^2} \tag{53}$$

In order to deduce an analytical backface velocity profile as a function of the applied pressure, σ_7 and σ_{10} are deduced from PDV 3, as shown in Section 5.2. Eq. (53) can be expressed as a function of time t as follows:

$$v_{BF}(t) = -\frac{4[Z_A - Z_B]P\left(t - \frac{3d_B}{c_B} - \frac{d_A}{c_A}\right)}{[Z_A + Z_B]^2} + \frac{4P\left(t - \frac{d_B}{c_B} - \frac{d_A}{c_A}\right)}{Z_A + Z_B}, \quad \forall t \in [t_2, t_m] - \frac{4P\left(t - \frac{d_B}{c_B} - 3\frac{d_A}{c_A}\right)[Z_A - Z_B]}{[Z_A + Z_B]^2} \tag{54}$$

Since, $\forall t \in [t_0, t_2]$, $P\left(t - \frac{3d_B}{c_B} - \frac{d_A}{c_A}\right) = 0$ and $P\left(t - \frac{d_B}{c_B} - 3\frac{d_A}{c_A}\right) = 0$, Eq. (54) can be simplified accordingly within that time interval, such as the analytical solution is defined piecewise with the following expressions:

$$v_{BF}(t) = \begin{cases} -\dfrac{4[Z_A - Z_B]\left(P\left(t - \frac{3d_B}{c_B} - \frac{d_A}{c_A}\right) + -P\left(t - \frac{d_B}{c_B} - 3\frac{d_A}{c_A}\right)\right)}{[Z_A + Z_B]^2} \\ \qquad + \dfrac{4P\left(t - \frac{d_B}{c_B} - \frac{d_A}{c_A}\right)}{Z_A + Z_B}, \quad \forall t \in [t_2, t_m] \\ \dfrac{4P\left(t - \frac{d_B}{c_B} - \frac{d_A}{c_A}\right)}{Z_A + Z_B}, \quad \forall t \in [t_0, t_2] \end{cases} \tag{55}$$

Figs. 17(a) and 17(b) present a comparison between the analytically predicted backface velocities and the experimental measurements for partially bonded pellets, in configurations 2 and 5. The overall agreement between the 1D elastodynamic model and the measured data is globally satisfactory until $t \simeq 0.75\,\mu s$, with only minor differences between both provided the various sources of discrepancies like errors of Lissajous post-processing of PDV signals (see Section 3.1), the 1D modeling of wave propagation, and the unmodeled thickness of the joint. At time $t \simeq 0.75\,\mu s$, the experimental and analytical curves clearly diverges from each other, and the predicted responses with no decohesion clearly yield a lower local minimum value of the backface velocity once the first maxima have been achieved, with respect to experimental signals. This divergence can be interpreted as the signature of the occurrence of failure, which is analog to what is observed in LASAT (Bolis et al., 2007) or spall fracture (Antoun et al., 2006). The creation of a new free surface is expected to make reincrease the backface velocity before the predicted minimum value in the no-decohesion scenario is reached. However, Figs. 17(a) and 17(b) both show a slight time delay between the times of divergence between both curves and of local minimum of the velocity. This phenomenon remains to be explained, and will require further effort in the future. Besides, the local minimum values of the backface velocity may not go back to zero if the applied load does not return to zero as well. For instance, the time evolution of the applied stress on configuration 5 shown in Fig. 16 does not go back to zero after its first extremum, which leads to the non-zero minimum velocity shown in Fig. 17(b). Conversely, the loading profile of configuration 2 does go back to zero in Fig. 16, whose image yields the zero value of the backface velocity shown in Fig. 17(a).

5.3. Application of Novikov's extended criteria to experimental outcomes

5.3.1. Identification of the tri-layer model on experimental outcomes

The identification of the velocity values $v_{\bar{m}}, v_{\bar{2}}, v_{m'}, v_{2'}, v_{2''}, v_{m''}$ from the time evolution of the experimental backface velocity essentially relies on the identification of its first local minimum, identified as $v_{m'}$ for the tri-layer model developed in Section 4.3. Next, the following

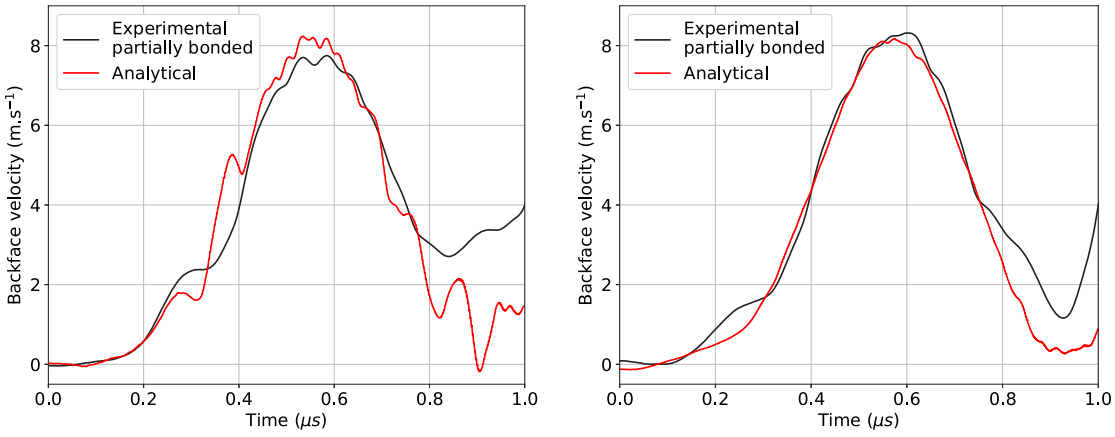

(a) Configuration 2 (b) Configuration 5

Fig. 17. Comparison between measured and analytically predicted backface velocities during Magnetic Pulse Disassembly tests conducted on configurations 2 and 5 on partially bonded assemblies.

Table 5
Identified velocities (rounded) values (m s^{-1}), and stresses (Pa) computed with the extended Novikov criterion for tri-layer modeling.

Config	$v_{\bar{2}}$	$v_{2'}$	$v_{2''}$	$v_{\bar{m}}$	$v_{m'}$	$v_{m''}$	σ_{iii}	σ_{ii}	$\sigma_{1'}$	σ_{iv}
2	2.19	2.19	2.24	2.71	2.7	2.71	-1.29×10^7	-1.20×10^7	-1.24×10^7	-1.17×10^7
3	2.81	2.92	3.03	1.68	1.58	1.72	2.57×10^7	2.77×10^7	2.82×10^7	3.07×10^7
5	4.03	4.23	4.44	1.17	1.16	1.16	6.12×10^7	6.56×10^7	6.34×10^7	6.59×10^7
2 full	2.99	3.04	3.09	0.55	0.54	0.54	6.51×10^7	6.76×10^7	6.64×10^7	6.78×10^7
3 full	6.27	6.17	6.16	2.01	1.9	1.98	9.78×10^7	9.7×10^7	10×10^7	9.78×10^7
5 full	2.69	2.78	2.86	3.14	3.13	3.15	-1.02×10^7	-8.54×10^6	-9.15×10^7	-8.03×10^6

time intervals

$$\Delta t_{\bar{m}-m'} = \Delta t_{\bar{2}-2'} = \frac{d_C}{c_C} \tag{56}$$

$$\Delta t_{\bar{2}-m'} = 2\frac{d_B}{c_B} + \Delta t_{\bar{m}-m'} \tag{57}$$

allow to identify the times where to extract the velocity values $v_{\bar{m}}, v_{\bar{2}}, v_{2'}$, $v_{2''}, v_{m''}$. For the moment, the current version of Novikov's extended criterion is restricted to configurations where the maximum tensile stress is localized at the interface between layers A and B, which corresponds to configurations 2, 3, and 5 (see Table 4). For configurations 1 and 4, analog but more detailed developments are required, similar to those performed in de Rességuier (2018, Sections 3.2 and 3.3), but which are not included in this work.

The wave speeds and the material wave impedances of layers B and C are extracted from Tables 2 and 3. Considering these data, the layer thicknesses listed in Table 4, and a joint of about 10 micrometers thick, the calculation of the time intervals (56) and (57) can be performed, required to extract the relevant backface velocity values, and the stresses can also be computed. It is important to note that Z_C was here assigned based on generic characteristics of epoxy. In a more in-depth study, it would be beneficial to investigate the specific behavior of the adhesive used in order to refine this parameter and enhance the model's reliability.

To illustrate the aforementioned identification procedure, the points reported in Table 5, although extracted from different curves, are plotted in Fig. 18 considering the configuration 1, serving as a representative example. Points $2', 2'', \bar{m}, m''$ provide additional information with respect to the bi-layer model that allows the estimate of intermediate stress values.

Next, Table 5 summarizes the relevant velocity values, as well as the estimated stress values given by the tri-layer model, both for the partially and fully bonded cases. Besides for readability purpose, Fig. 19 shows an histogram of stress values computed for various configurations.

Several key observations can be made. First, the fracture stresses are generally of the order of tens of MPa. This is consistent for instance with metal hybrid polymers with Cu and Al (Frick et al., 2022). Second, non-physical negative values of fracture stresses are obtained for configurations 2 and $5full$. Such case appears when the minimum velocity value $v_{m'}$ occurs too early, that is the hump width is lower than for other configurations. Hence, the points $\bar{2}$, $2'$ and $2''$ might have a lower velocity value than $\bar{m}$, m' and m'' resulting in negative computed stress values. Therefore the model, in its current form, cannot be used to analyze these signals, as other phenomena may have occurred for which further analysis is required, but which go beyond the purpose of the present work. Third, for configurations $2full$ and 5, no significant difference is observed between stress values in partially and fully bonded cases, as shown in Fig. 19. The estimated reconstructed stress values, either related to adhesive (point ii, iii, iv) or cohesive (point $1'$) failure modes, are consistent with Fig. 14 since they are ordered as $\sigma_{\text{iv}} > \sigma_{\text{ii}} > \sigma_{1'} > \sigma_{\text{iii}}$ for optimal configurations. Therefore, the analytical results indicate that the highest possibly achievable stress in these configurations correspond to a potential failure at point iv. Such a failure is adhesive in nature, with the adhesive layer remaining bonded to layer A. This result is consistent with post-mortem observations shown in Fig. 6, associated with partially bonded pellets, that clearly reveal an adhesive failure in which the adhesive layer remains bonded to layer A. Moreover, since configuration 5 was designed to be a repetition of configuration 2, a consistency between their recomputed stress values was expected, and is actually also what is observed between 5 and $2full$. Fourth, configuration 3 and $3full$ show values of failure strength which are significantly different, with maximum stresses in states iv and $1'$ respectively. Notice also that the computation of stress states iii, $1'$, ii, iv can also be affected of some error if the signal of backface velocity is affected of high frequency noise, as it seems to be the case for configurations 3 and $3full$, see Figs. 9(a) and 9(c). Besides, since

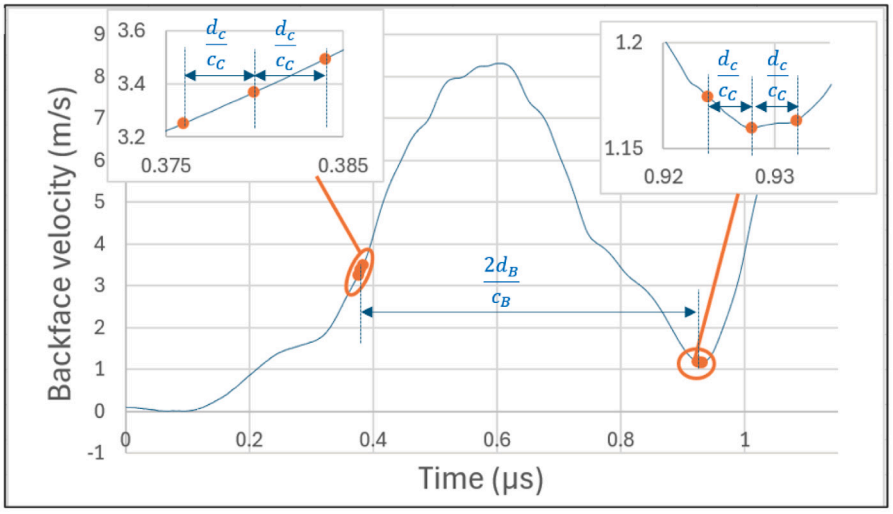

Fig. 18. Illustration of the identification method on Configuration 1.

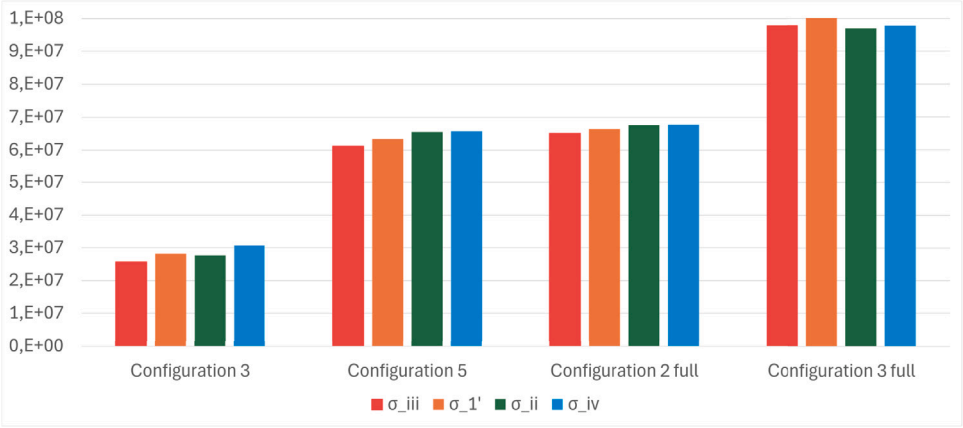

Fig. 19. Histogram of recomputed stresses (Pa) in the tested configurations, from the tri-layer model.

the adhesive was applied manually, variations in its tensile strength between tests are not surprising.

Overall, the computation of such a sequence of stress values provides insight regarding stress states that may have been sustained by the adhesive joints before it fails. This sequence allows to define a bounded range for the fracture stress of the adhesive joint, lying in between σ_{iii} and σ_{iv}, corresponding respectively to the lowest and highest stress values leading to failure at the outermost interfaces.

5.3.2. *Application of the bi-layer model to experimental outcomes*

As for the tri-layer model, the identification of the values v_m and $v_{\bar{2}}$ from the time evolution of the experimental backface velocity essentially relies on the identification of its first local minimum, identified as v_m in Eq. (10), associated with the bi-layer model. Next, the following time interval

$$\Delta t_{\bar{2}-m} = 2\frac{d_B}{c_B} \tag{58}$$

allows us to identify the time where to extract the velocity value $v_{\bar{2}}$. Table 6 summarizes the relevant velocity values, as well as the estimated fracture stresses recomputed with the same values of physical parameters than these already used for the tri-layer model.

First, the same comment can be made regarding the non-physical recomputed negative stress values for configurations 2 and $5\,full$, which come from an identified negative velocity difference $v_{\bar{2}} - v_m$ on the respective experimental signals. Second, it is observed that $\sigma_{\bar{1}}$, computed with the bi-layer model, has the same value as σ_{iv}, computed with the tri-layer model. One thus concludes that points iv and $\bar{1}$ drawn on the generic sketch shown in Fig. 14 are almost superposed in the tested configurations. It means that only one wave round trip within the adhesive layer was sufficient to debond it.

Table 6
Identified velocities (rounded) values (m s^{-1}), and stresses (Pa) computed with the extended Novikov criterion for bi-layer modeling.

Config	$v_{\bar{2}}$	v_m	$\sigma_{\bar{1}}$
2	2.19	2.70	-1.17×10^7
3	3.40	2.52	2.02×10^7
5	4.23	1.16	6.59×10^7
2 full	3.04	0.54	6.78×10^7
3 full	3.48	2.85	2.27×10^7
5 full	2.78	3.13	-8.03×10^6

6. Conclusion

This paper has presented an experimental proof-of-concept of magnetic pulse disassembly, conducted on adhesively bonded Aluminum 2017 T4-MARS 300 specimen, using the GEPI pulse system from CEA Gramat. This generator was selected for its suitable high current frequency, ensuring sufficiently short rise time, of the order of 550 ns,

which allows magnetic pulse disassembly of millimeter-thick assemblies. It was however used close to its lower bound of pressure in order to avoid damaging the disassembled layers.

Ten interfacial assembly conditions were selected, including partially bonded (localized adhesive spots) and fully bonded assemblies. During the disassembly tests, the backface velocity of each configuration, as well as that of the electrode, was systematically measured. Experimental observations confirmed that adhesive failure had occurred at the interface. For partially bonded specimens, the center of the adhesive joint remained attached to the electrode, while the peripheral areas adhered to the pellet. Conversely, for fully bonded specimens, the adhesive layer detached entirely from the electrode and adhered fully to the pellet. These distinct failure patterns underline significant differences in the response of assemblies between partially and fully bonded configurations under magnetic pulse loading.

Then, two analytical models based on bi-layer and tri-layer assemblies were used to provide estimates of the interface fracture strength of the assemblies. These estimates provide lower and upper bounds of the sought interfacial fracture strength, so that to frame it. These estimates extend Novikov's basic criterion to multi-material assemblies in the context of time continuous loading. The first estimate reads similar to Novikov's basic criterion, but computed with an early-in-time extracted velocity value $v_{\tilde{2}}$, ahead of the maximal backface velocity value. The second estimate is based on a two-scale in time characteristic analysis, considering a thickened adhesive layer, and providing intermediate cohesive and adhesive stress states, which are potential candidates for failure. These estimates were applied only to configurations 2, 3, and 5, where maximum tensile stresses are localized at the interface of the assembly.

The proof-of-concept of magnetic pulse disassembly is here validated, on the one hand via the ability of the linear elastodynamic modeling of the bilayer laminate to correctly predict the measured backface velocity up to the onset of interfacial failure, showing that experiments behave as expected; on the other hand, the interface's fracture strength of the assembly can be estimated from the measurements of the backface velocity and the constructed estimates. However, this work opens many perspectives of various natures. From an experimental perspective, a larger database should be constructed, to explore other configurations, test more resistant interfaces, like for instance welded or brazed assemblies. It may allow to build a database of fracture strength values obtained for various geometrical and material configurations, and also determine what is the lower bound for the process. From an industrial perspective, magnetic pulse disassembly clearly requires fast, but less powerful and more compact generators than GEPI, that could be transposed to a disassembly line. From the modeling perspective, the design of next experimental tests and the interpretation of measured backface velocities should be supplemented with 1D and 3D numerical simulations, especially to better understand and quantify cross-sectional effects due the geometry of the joint. Overall, the proposed approach provides a methodology to design assemblies, which are disassemblable under magnetic pulse loading, consistently with the context of sustainable engineering. It also opens new perspectives for reversible joining technologies and end-of-life recycling applications.

CRediT authorship contribution statement

Benoit Lagain: Writing – review & editing, Writing – original draft, Visualization, Methodology, Investigation, Formal analysis, Data curation, Conceptualization. **Thomas Heuzé:** Writing – review & editing, Writing – original draft, Visualization, Validation, Supervision, Resources, Project administration, Methodology, Investigation, Funding acquisition, Formal analysis, Data curation, Conceptualization. **Guillaume Racineux:** Writing – review & editing, Validation, Supervision, Resources, Project administration, Funding acquisition. **Michel Arrigoni:** Writing – review & editing, Validation, Supervision, Funding acquisition. **Sébastien Bergey:** Software, Resources, Data curation. **Thibaut Paccou:** Conceptualization, Data curation, Software, Writing – review & editing. **Camille Chauvin:** Writing – review & editing, Validation, Funding acquisition, Conceptualization.

Declaration of competing interest

The authors declare that they have no known competing financial interests or personal relationships that could have appeared to influence the work reported in this paper.

Acknowledgments

Benoit Lagain is funded on the one hand by Agence de l'Innovation de Défense (AID) grant reference number 2021 65 0044, and on the other hand by Ecole Centrale de Nantes. The authors also thank CEA Gramat, France, for their support during the experimental test campaign. A CC-BY public copyright license has been applied by the authors to the present document and will be applied to all subsequent versions up to the Author Accepted Manuscript arising from this submission, in accordance with the grant's open access conditions.

Data availability

Data will be made available on request.

References

Antoun, T., Seaman, L., Curran, D.R., Kanel, G.I., Razorenov, S.V., Utkin, A.V., 2006. Spall Fracture. Springer Science & Business Media.

Blanc, G.L., Chanal, P.-Y., Héreil, P.L., Laporte, P., Avrillaud, G., Vincent, P., L'eplattenier, P., 2008. Ramp wave compression in a copper strip line: Comparison between mhd numerical simulations (LS-DYNA®) and experimental results (GEPI device).

Bolis, C., Berthe, L., Boustie, M., Arrigoni, M., Barradas, S., Jeandin, M., 2007. Physical approach to adhesion testing using laser-driven shock waves. J. Phys. D: Appl. Phys. 40 (10), 3155.

Boustie, M., Cuq-Lelandais, J., Bolis, C., Berthe, L., Barradas, S., Arrigoni, M., De Resseguier, T., Jeandin, M., 2007. Study of damage phenomena induced by edge effects into materials under laser driven shocks. J. Phys. D: Appl. Phys. 40 (22), 7103.

de Rességuier, T., 2018. On the shock-based determination of the adhesive strength at a substrate-coating interface. J. Adhes. Sci. Technol. 32 (1), 36–49.

Frick, A., Rettenberger, M., Spadaro, M., 2022. Evaluation of the interfacial adhesion between polymer and metal on polymer-metal hybrids. Polym. Test. 106, 107448.

Gay, E., Berthe, L., Boustie, M., Arrigoni, M., Buzaud, E., 2014a. Effects of the shock duration on the response of CFRP composite laminates. J. Phys. D: Appl. Phys. 47 (45), 455303.

Gay, E., Berthe, L., Boustie, M., Arrigoni, M., Trombini, M., 2014b. Study of the response of CFRP composite laminates to a laser-induced shock. Compos. Part B: Eng. 64, 108–115.

Hereil, P., Lassalle, F., Avrillaud, G., 2004. GEPI: an ice generator for dynamic material characterisation and hypervelocity impact. In: AIP Conference Proceedings, vol. 706, (1), American Institute of Physics, pp. 1209–1212.

Kapil, A., Sharma, A., 2015. Magnetic pulse welding: an efficient and environmentally friendly multi-material joining technique. J. Clean. Prod. 100, 35–58.

Kormpos, P., Unaldi, S., Berthe, L., Tserpes, K., 2023. A laser shock-based disassembly process for adhesively bonded Ti/CFRP parts. Processes 11 (2), 506.

Lagain, B., Heuzé, T., Racineux, G., Arrigoni, M., 2023a. An analytical approach of design for recycling of laminate structures by the use of magnetic pulse disassembling. Int. J. Solids Struct. 112290.

Lagain, B., Heuzé, T., Racineux, G., Arrigoni, M., 2023b. Numerical analysis of cross-sectional effects during the magnetic pulse disassembly of laminate structures. Adv. Eng. Mater. 25 (20), 2300728.

Laporte, D., 2011. Analyse de la réponse d'assemblages collés sous des sollicitations en dynamique rapide. Essais et modélisations (Ph.D. thesis). ISAE-ENSMA Ecole Nationale Supérieure de Mécanique et d'Aérotechique-Poitiers.

Luminita, C., Arrigoni, M., Deleanu, L., Istrate, M., 2018. Assessment of delamination in tensylon® uhmwpe composites by laser-induced shock. Mater. Plast. 55 (3).

Mercier, P., Benier, J., Azzolina, A., Lagrange, J., Partouche, D., 2006. Photonic doppler velocimetry in shock physics experiments. In: Journal de Physique IV (Proceedings), vol. 134, EDP sciences, pp. 805–812.

Novikov, S., Divnov, I., Ivanov, A., 1966. The study of fracture of steel, aluminum, and copper under explosive loading. Phys. Met. Metal Sci. (USSR) 21 (4), 608–615.

Sun, H., Kosukegawa, H., Takagi, T., Uchimoto, T., Hashimoto, M., Takeshita, N., 2021. Electromagnetic pulse-induced acoustic testing and the pulsed guided wave propagation in composite/metal adhesive bonding specimens. Compos. Sci. Technol. 201, 108499.

Tahan, G., Arrigoni, M., Bidaud, P., Videau, L., Thévenet, D., 2020. Evolution of failure pattern by laser induced shockwave within an adhesive bond. Opt. Laser Technol. 129, 106224.

Takagi, A., Kimoto, Y., Shinozaki, A., Yamada, H., Kojima, T., Yonezu, A., 2024. Development of LaSAT and bonding strength evaluation of epoxy adhesive over a wide range of loading rates. J. Adhes. 100 (7), 576–598.

Wang, L., 2011. Foundations of Stress Waves. Elsevier.

Weng, J., Tan, H., Wang, X., Ma, Y., Hu, S., Wang, X., 2006. Optical-fiber interferometer for velocity measurements with picosecond resolution. Appl. Phys. Lett. 89 (11).